Absolute total and one- and two-electron transfer cross sections for Ar^{q+} ($8 \le q \le 16$) on He and H_2 at $2.3q$ keV

J. Vancura, V. J. Marchetti, J. J. Perotti, and V. O. Kostroun

Nuclear Science and Engineering Program, Ward Laboratory, Cornell University, Ithaca, New York 14853

(Received 20 August 1992)

Absolute values for the total and one- and two-electron transfer cross sections for Ar^{q+} ions ($8 \le q \le 16$) colliding with helium and molecular hydrogen at $2.3q$ keV laboratory energy were measured by the growth-rate method. The He and H_2 total cross sections as a function of Ar-projectile L-shell occupation number increase monotonically from Ar^{8+}, $2p$ shell full, to Ar^{16+}, $2s$ shell empty. The H_2 one-electron capture cross section scales approximately as $[E_{IP}(He)/E_{IP}(H_2)]^2$ times the corresponding He cross section, but the shapes of the two cross sections differ in detail. The Ar^{q+} ions were produced by the Cornell superconducting-solenoid, cryogenic electron-beam ion source (CEBIS) and extracted at 2.3 kV. Selected charge states traversed a gas cell, after which they were detected and charge-state analyzed by the energy-retardation method and by a $\pi/\sqrt{2}$ cylindrical electrostatic analyzer. The target-gas pressure in the cell was measured directly by the orifice-flow method used for absolute-pressure gauge calibration. The overall error in the Ar^{q+} on H_2 cross-section measurements is $\pm 10\%$, and $\pm 15\%$ in the He measurements.

I. INTRODUCTION

In recent years, there has been increasing interest in the interactions of low-energy, very-highly-charged ions with atomic and molecular hydrogen and helium. Such interactions play a role in laboratory and astrophysical plasmas, and accurate and reliable atomic data characterizing such interactions are needed for plasma modeling and the quantitative interpretation of diagnostic measurements. From a theoretical standpoint, collisions of bare, one- and two-electron ions of low to medium Z with simple atoms and molecules are of interest because of the possible calculational tractability of such systems, and the relatively small number of unambiguous physical processes that can take place in such collisions. In spite of the availability in recent years of advanced ion sources of the electron cyclotron resonance (ECRIS) [1] and electron beam (EBIS) [2] types which are capable of producing low-energy, very-highly-charged ions, direct measurements of absolute cross sections for ion charge states greater than ten are still quite rare. A few experiments involving collisions of low-velocity ($v \ll 1$ a.u.), very-highly-charged ions and atoms or simple molecules have been reported in the literature. These are Ne^{q+} ($2 \le q \le 8$), Ar^{q+} ($7 \le q \le 9$), Kr^{q+} ($2 \le q \le 13$), and Xe^{q+} ($2 \le q \le 13$) projectiles on He, at energies between 0.25 and $1.00q$ keV, Justiniano *et al.* [3]; Kr^{q+} ($7 \le q \le 25$) on He at $1.0q$ keV, Iwai *et al.* [4]; I^{q+} ($10 \le q \le 41$) on He at $1.25q$ keV, Tawara *et al.* [5]; Ne^{q+} ($2 \le q \le 7$) on H_2 and Ar^{q+} ($2 \le q \le 10$) on H_2 at $2.0q$ keV, Can *et al.* [6]; Ar^{q+} ($4 \le q \le 15$) and I^{q+} ($5 \le q \le 27$) on He and H_2 at $0.198q$ keV, Mann [7]; Xe^{q+} ($11 \le q \le 31$) on He at $4.0q$ keV, Andersson, Astner, and Cederquist [8]; and Xe^{q+} ($11 \le q \le 35$) on Xe at $4.0q$ keV, Cederquist *et al.* [9].

In this paper, we report on the measurement of the absolute total and one- and two-electron transfer cross sections for Ar^{q+} ($8 \le q \le 16$) on He at H_2 at $2.3q$ keV. The measured one- and two-electron transfer cross sections include all processes which result in an argon-projectile final charge state that is one or two units lower than the incident charge state. Argon projectiles and the two-electron targets He and H_2 were selected to investigate in detail the processes of double-electron capture and transfer ionization for projectile charge states $q \ge 10$.

II. EXPERIMENTAL METHOD

The basic experimental methods and associated techniques for determining charge changing cross sections for hydrogen beams passing through gases are described in a review article by Tawara and Russek [10]. These can be taken over directly to measure charge transfer cross sections for low-energy, highly charged ions, provided certain considerations are taken into account. These considerations are necessary because the cross sections of interest are large, 10^{-15}–10^{-14} cm^2, there is a number of possible paths that can lead to a given final charge state, and the efficiency of ion detection can vary with projectile charge state due to secondary electron emission when highly charged ions strike surfaces.[11]

In this work, the absolute total and one- and two-electron transfer cross sections were measured by the growth-rate method [10]. In this method, a beam of ions of charge q traverses a gas cell of length l and of target density n /cm^3. Due to charge changing collisions, new charge state fractions are produced. The growth of the different ion charge states with increasing pressure and the decrease of the incident projectile charge state are recorded. The cross sections are determined from the

measured charge state versus pressure dependence.

Following a collision with a two-electron target atom, the charge state q of the projectile can either remain the same, or change to $q-1$ or $q-2$. While the change in charge corresponding to $q-2$ can, in principle, be attributed directly to two-electron transfer from the target to the projectile, it is not possible to say whether the final charge state $q-1$ is due to one-electron capture or to two-electron capture into states of the projectile that decay by autoionization and which change the charge on the projectile by one unit instead of by two.

If we let $\sigma_{q,q-1}$ and $\sigma_{q,q-2}$ represent the true one- and two-electron capture cross sections for an ion of charge q, and $a_{2,1}^{q-2}$ the probability that the charge state $q-2$ formed by two-electron capture decays by nonradiative transitions, then the effective charge transfer cross section $\sigma'_{q,q-1}$ is given by $\sigma'_{q,q-1}=\sigma_{q,q-1}+a_{2,1}^{q-2}\sigma_{q,q-2}$. If more than one collision in the cell is allowed, then the charge state q which changed into $q-1$ by direct one-electron capture with cross section $\sigma_{q,q-1}$, or by two-electron capture followed by autoionization with effective cross section $a_{2,1}^{q-2}\sigma_{q,q-2}$, can, in turn, change into $q-2$ and $q-3$, etc., by the paths shown in Fig. 1. We also assume that for the higher projectile charge states, in addition to one-electron capture, two-electron capture followed by autoionization occurs with an unknown but not insignificant probability. This assumption is based on the idea that excited states involving two electrons will decay nonradiatively by Auger emission, and also on experiments carried out by Cocke et al. [12] with 0.5q-keV Ar^{q+} ($2 \leq q \leq 9$) on He.

The resulting equations that describe the evolution of the charge state distribution with gas-target thickness $\rho=nl$ are then
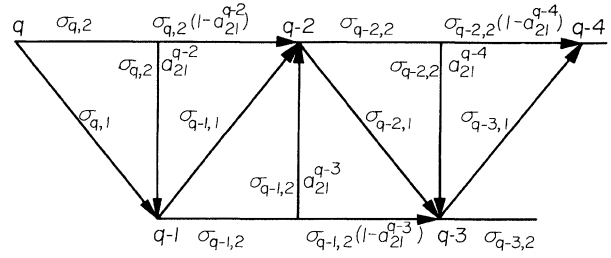

FIG. 1. Pathways that can lead to a given charge state ξ of a projectile assuming only direct one- and two-electron capture, and autoionization of excited states of the projectile formed in two-electron capture with probability $a_{\xi,1}^{\xi}$.

$$\frac{dN_q}{d\rho}=-N_q\sigma'_{q,t} \ ,$$

$$\frac{dN_{q-1}}{d\rho}=N_q\sigma'_{q,1}-N_{q-1}\sigma'_{q-1,t} \ ,$$

$$\frac{dN_{q-2}}{d\rho}=N_q\sigma'_{q,2}+N_{q-1}\sigma'_{q-1,1}-N_{q-2}\sigma'_{q-2,t} \ ,$$ (1)

$$\frac{dN_{q-3}}{d\rho}=N_{q-1}\sigma'_{q-1,2}+N_{q-2}\sigma'_{q-2,1}-N_{q-3}\sigma'_{q-3,t} \ ,$$

with $\sigma_{q,t}\equiv\sigma'_{q,t}\equiv\sigma_{q,q=1}+\sigma_{q,q-2}$, $\sigma'_{q,1}\equiv\sigma_{q,q-1}+a_{2,1}^{q-2}\sigma_{q,q-2}$, $\sigma'_{q,2}\equiv\sigma_{q,q-2}(1-a_{2,1}^{q-2})$, etc. For reasonable gas-target thicknesses, we only need to consider two collisions at most for a given incident ion, in which case only the first three equations in (1) are retained. This system of equations can be solved by the method of Laplace transforms, with the result that

$$N_q(\rho)=N_q(0)e^{-(\sigma'_{q,t}\rho)} \ ,$$

$$N_{q-1}(\rho)=\frac{\sigma'_{q,1}}{(\sigma'_{q-1,t}-\sigma'_{q,t})}\{e^{-(\sigma'_{q,t}\rho)}-e^{-(\sigma'_{q-1,t}\rho)}\}N_q(0) \ ,$$ (2)

$$N_{q-2}(\rho)=\frac{\sigma'_{q-1,1}\sigma'_{q,1}-\sigma'_{q,2}(\sigma'_{q,t}-\sigma'_{q-1,t})}{(\sigma'_{q,t}-\sigma'_{q-1,t})(\sigma'_{q,t}-\sigma'_{q-2,t})}\{e^{-(\sigma'_{q,t}\rho)}\}N_q(0)-\frac{\sigma'_{q-1,1}\sigma'_{q,1}}{(\sigma'_{q,t}-\sigma'_{q-1,t})(\sigma'_{q-1,t}-\sigma'_{q-2,t})}\{e^{-(\sigma'_{q-1,t}\rho)}\}N_q(0)$$

$$+\frac{\sigma'_{q-1,1}\sigma'_{q,1}+\sigma_{q,2}(\sigma'_{q-1,t}-\sigma'_{q-2,t})}{(\sigma'_{q,t}-\sigma'_{q-2,t})(\sigma'_{q-1,t}-\sigma'_{q-2,t})}\{e^{-(\sigma'_{q-2,t}\rho)}\}N_q(0) \ .$$

If we assume that $(\sigma_{q,t}\rho)$, $(\sigma_{q-1,t}\rho)$, and $(\sigma_{q-2,t}\rho)$ are all $\ll 1$, the above equations become, to second order in ρ,

$$\frac{N_q(\rho)}{N_q(0)}=1-\sigma_{q,t}\rho+\tfrac{1}{2}(\sigma_{q,t}\rho)^2 \ ,$$

$$\frac{N_{q-1}(\rho)}{N_q(0)}=\sigma'_{q,1}\rho-\tfrac{1}{2}\sigma'_{q,1}(\sigma_{q,t}+\sigma_{q-1,t})\rho^2 \ ,$$ (3)

$$\frac{N_{q-2}(\rho)}{N_q(0)}=\sigma'_{q,2}\rho+\tfrac{1}{2}\{\sigma'_{q,1}\sigma'_{q-1,1}$$

$$-\sigma'_{q,2}(\sigma_{q,t}+\sigma_{q-2,t})\}\rho^2 \ .$$

These equations underlie the experimental measurements of cross sections by the growth method in the present experiment.

A. Experimental arrangement

Low-energy, highly charged argon ions were produced by the Cornell superconducting-solenoid, cryogenic electron-beam ion source CEBIS [13]. In an EBIS, highly charged ions are produced by sequential electron impact ionization of ions trapped in a high-current-density electron beam confined by a solenoidal magnetic field. The ions are trapped radially by the space-charge potential of

the electron beam and axially by an electric potential distribution applied to cylindrical electrodes concentric with the beam. After a predetermined confinement time, the potential distribution applied to the cylindrical electrodes is changed to extract the ions from the source. The resulting ion current pulse is a few tens of microseconds long. In the present experiment, ions were produced by a 17-mA, 3.8-keV electron beam (-1.5 kV on the electron gun cathode, and $+2.3$ kV applied to the cylindrical electrode drift tube structure). The confinement times ranged from 40 to 100 ms.

After extraction, the ions were charge analyzed by a 90° bending magnet and entered a gas cell. After exiting from the gas cell, the ion beam was again charge state analyzed either by a system of retarding grids or by a $\pi/\sqrt{2}$ cylindrical electrostatic analyzer with 1.0-mm-wide entrance and exit slits. The ions were detected by a shielded Faraday cup located behind the retarding grids, or by a high-current channeltron electron multiplier placed behind the $\pi/\sqrt{2}$ analyzer exit slit, Fig. 2. The $\pi/\sqrt{2}$ analyzer and Faraday cup were mounted on a translation stage that moved perpendicular to the incident beam direction. The translation stage lead screw was attached to an ultrahigh-vacuum rotary feed through, and the stage could be moved either manually or by a stepper motor.

The ion current pulses detected either by the Faraday cup or the channeltron were amplified by a Keithley Model 427 current-to-voltage amplifier. The output of this amplifier was fed to a Tektronix 2430A digital oscilloscope, which averaged the pulses over a predetermined number of extracted EBIS ion pulses, and integrated them over time. The integral of the averaged pulses, together with other information such as the pressures in the gas cell and the main vacuum chamber, and the retarding grid or cylindrical analyzer voltages were all recorded with the help of an IBM Model 30/286 personal computer data-acquisition system.

The main vacuum chamber was pumped on by a 170 l/s Balzers turbomolecular pump and 1000 l/s Varian VK12A cryopump. The base pressure in the system was 1.0×10^{-9} mbar. At the highest pressure (4.2×10^{-5} mbar) used in the gas cell, the pressure in the main vacuum chamber was 4.5×10^{-7} mbar with He and 3×10^{-8} mbar with H_2. Although the pumping speed and capacity of the cryopump for He are 50 l/s and 8 mbar l at

FIG. 2. Experimental arrangement used in the measurements of cross sections.

1.33×10^{-6} mbar, respectively, the cryopump and turbomolecular pump combination proved adequate, provided that the cryopump was periodically and briefly warmed up to discharge the He. The gas-handling system was constructed from stainless steel and is bakeable to 200 °C. The 99.999%-purity helium and 99.995%-purity hydrogen gas passed through a liquid-nitrogen cold trap to remove impurities before entering the gas cell. Whenever the gas was changed, the system was baked and flushed out with the working gas several times.

B. The gas cell

In order to measure the effective gas-cell-target thickness, the absolute pressure in the cell has to be known. In general, the uncertainty in pressure is one of the major sources of error in cross-section measurements [10]. The pressure can be measured directly by a McLeod gauge, by a capacitance manometer, by a spinning rotor friction gauge, or by a gauge calibrated against a standard. Because of the relatively large cross sections for processes involving highly charged ions, the pressures in the gas cell have to be low and hence preclude the use of McLeod gauges and capacitance manometers. At pressures on the order of 10^{-5} mbar, the McLeod gauge can be used to measure pressures with difficulty and an uncertainty of $\pm 6\%$ [14], while capacitance manometers with a full scale pressure range of 1.333 mbar can have a total uncertainty of 50% of reading at these pressures [15]. The spinning rotor friction gauge is an expensive instrument, not commonly available in small laboratories, which leaves commercially available calibrated hot-cathode ionization gauges as an alternative to absolute pressure measurements. The gauges usually are calibrated for Ar and N_2, and the calibration procedure requires that the complete unit, controller, tube, and cables be calibrated as one. Furthermore, the gauges have to be checked at regular intervals, and calibration transfers to He and H_2 introduce further uncertainties.

Due to these considerations, we decided to design a gas cell in which the target-gas absolute pressure can be measured directly. The pressure measurement is based on the orifice-flow method used for absolute pressure gauge calibration [14,16]. In this method, a steady and calculable pressure is produced in a chamber by balancing the rate of flow of gas into this chamber against the rate of gas removal. The gas cell, shown schematically in Fig. 3, consists of two cylindrical chambers, of which the lower chamber is the target cell. The conductances of the ion beam entrance and exit apertures are added to give a total conductance C_2. Target gas is admitted by a leak valve into the upper chamber, separated from the lower chamber by a very small conductance C_1. The absolute pressure P_1 of the gas contained in the upper chamber is measured by a capacitance manometer. In the molecular-flow regime, the gas flow through conductance C_1 into the lower chamber is

$$Q_1 = C_1(P_1 - P_c) , \tag{4}$$

where P_c is the pressure in the lower chamber. At equilibrium and constant throughput, the gas flow through
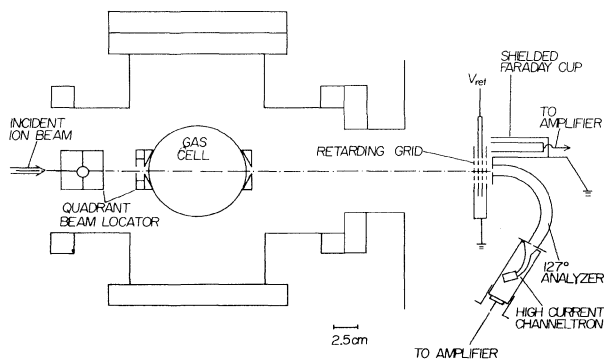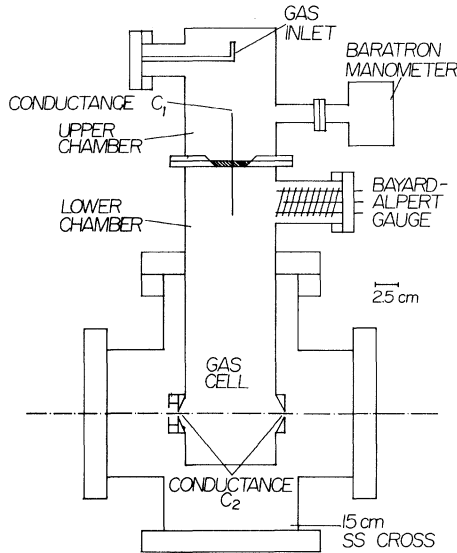
FIG. 3. Schematic of gas-target cell. The absolute pressure in the gas cell is measured by the orifice-flow method. SS denotes stainless steel. For details see text.

the lower chamber entrance and exit apertures into the experimental vacuum chamber is

$$Q_2 = C_2(P_c - P_e) ,$$ (5)

where P_e is the pressure in the vacuum chamber. Since the two conductances C_1 and C_2 are in series, $Q_1 = Q_2$, and the desired pressure P_c in the gas cell is given by

$$P_c = \frac{C_1 P_1 + C_2 P_e}{C_1 + C_2} .$$ (6)

In this design $C_2 P_e \ll C_1 P_1$, and since C_1 and C_2 can be calculated, the pressure P_c is given by

$$P_c = \frac{C_1 P_1}{C_1 + C_2} .$$ (7)

For molecular flow the conductance C is related to the absolute temperature T and gas molecular weight M by [17]

$$C = \alpha \left[\frac{T}{M} \right]^{1/2} ,$$ (8)

where α is a constant independent of the gas. Therefore, the ratio of the conductances C_1/C_2 is independent of the gas, and once determined can be used for other gases (provided that the gas temperature is the same at the two conductances).

Following the design of calibration systems [14,16], the gas cell has no extra tubing or elbows, and apart from the small conductances C_1 and C_2, all other pertinent conductances are very large. The gas inlet and all gauges are so located that entering gas molecules have to undergo at least one collision with the chamber wall.

For target-cell pressures in the range $10^{-6} - 10^{-4}$ mbar, the ratio of the two conductances C_1/C_2 has to be on the order of 10^{-5} if P_1 is to be in the range 0.1–10 mbar.

The lower chamber of the target cell is a stainless-steel (SS) cylinder, 9.84 cm in diameter, and 33 cm long. The cylinder is welded to a 20-cm-diam metal gasket sealed flange which attaches it to the experiment vacuum chamber, a 20-cm-diam, six-way stainless-steel cross. The entrance and exit aperture diameters are 0.4 and 0.5 cm, respectively, and 0.05 cm thick. They define a 12.2-cm-long path through the cell. Using the expression given by Berman [17], the calculated conductance for helium at 18 °C of the two apertures in series is 8.98 l/s. At the upper end of this chamber are a pumpout port and two ports, one for a nude Bayard-Alpert gauge and a spare port that can be used for gauge calibration. The upper chamber is also a stainless-steel cylinder, 9.84 cm in diameter and 17 cm long. The volume of the upper chamber, including all tubing and ports is 1380 ± 10 cm^3. The conductance C_1 which separates the upper chamber from the lower is a 14.2-cm-long piece of stainless-steel hypodermic tubing, 0.0813 cm outside diameter and 0.0508 ± 0.0051 cm inside diameter. The calculated conductance for helium according to the expression given in Ref. [17] is $(2.97 \pm 0.90) \times 10^{-4}$ l/s.

Unfortunately, the error in the calculated conductance C_1 is much too large, and therefore this conductance had to be measured experimentally. The upper chamber was filled with gas, and the pressure measured as a function of time as gas was removed through the much larger conductance C_2. The absolute pressure in the upper chamber was measured with a capacitance manometer, MKS Baratron model 222B [18]. From the slope of the pressure versus the time curve in the linear (molecular-flow) region, and the known volume of the upper chamber, the conductance C_1 was obtained. Figure 4 shows such a plot for helium. The experimentally measured value of C_1 for helium is $(2.89 \pm 0.03) \times 10^{-4}$ l/s, which compares well with the calculated value. From the experimentally measured valued of C_1 for H_2, He, and N_2, together with calculated values of C_2 for these gases, $C_1/C_2 = (3.24 \pm 0.06) \times 10^{-5}$. From Eq. (7), this ratio, together with the absolute pressure P_1, determines the pressure P_c in the gas cell.

In order to verify that the pressure P_e in the vacuum chamber was small compared to P_c, two nude Bayard-Alpert gauges (Granville Phillips type 271 [19]) were placed side by side in the vacuum system with the gas cell removed, and their readings compared over a pressure range of three decades. One of the gauges was then connected to the lower chamber of the gas-cell-calibration system and calibrated at pressures in the cell for which the other ionization gauge, connected to the vacuum system, recorded pressures at least 100 times lower. During the cross-section measurements, the gauge in the lower chamber of the gas cell was turned off in order to avoid its pumping [16]. The error in the absolute pressure P_c in the cell is estimated to be 2.5%, and consists of an uncertainty of 1.5% in the reading of the capacitance manometer, and a 2% uncertainty in the conductance ratio C_1/C_2.

The major uncertainty in determining the gas-target thickness is the effective length of the gas cell. The gas density in the vicinity of the ion beam entrance and exit
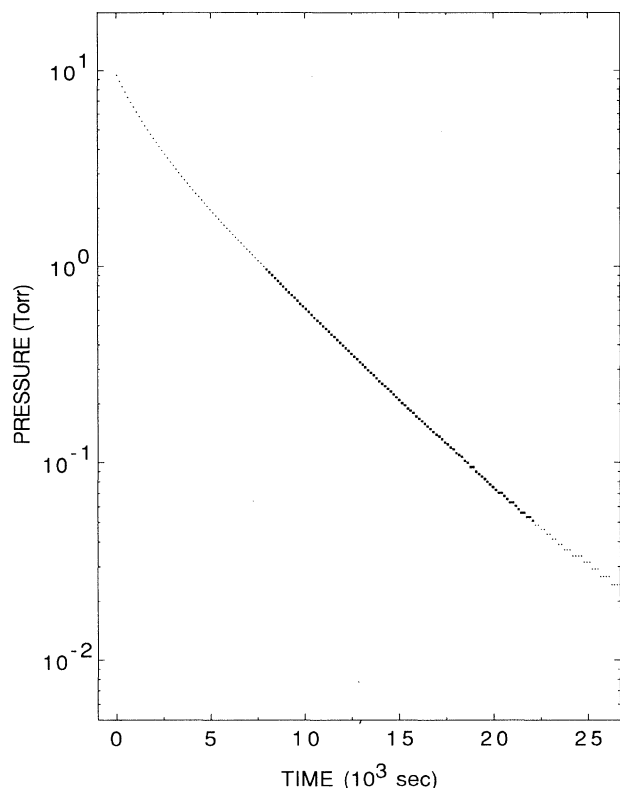
FIG. 4. Plot of helium of pressure P in the upper chamber of the gas cell vs time t in the linear (molecular flow) region. From the known volume V of the upper chamber and the slope of this curve, the conductance C_1 was obtained from the relation $\ln P = \ln P_0 - C_1 t / V$.

apertures does not drop off abruptly, but falls off gradually, both inside and outside the cell, due to gas effusing from the apertures. The problem of effective length was not investigated in this work, and for pressures in the vacuum system three orders of magnitude smaller than the pressure in the gas cell, we took the effective length to be the length of the gas cell plus the sum of the entrance and exit aperture diameters [20]. This introduces a maximum uncertainty of 7.4% in the gas-target thickness. With He in the cell, the ratio of vacuum system to gas-cell pressure was 1.25×10^{-2}, and in this case, we took the path length to be the distance from the 90° bending magnet focus to the ion detector, less the length of the gas cell, or 58 cm. (The ion optics of our beam line are such that only ions focused by the 90° analyzing magnet can make it through the cell.) This increased the effective length by 0.7 cm, and the uncertainty in the gas-target thickness for He was 13%.

C. Ion beam measurements

Purity of the ion beam is an important consideration in cross-section measurements. The presence of metastable states is known to influence measured cross sections [10,21]. The highly charged ion beams ($q \geq 8$) extracted from an EBIS are unlikely to contain metastables since the ions are formed by sequential electron impact ioniza-

tion [22]. Also, any metastables formed in the source are unlikely to survive bombardment by the few hundred A/cm^2 electron beam during the 40 ms or longer confinement time.

Contamination of the incident ion beam by ions of the same charge to mass ratio, e.g., O^{4+} and Ar^{10+}, is possible and was observed. In some measurements, the Ar^{10+} +He cross sections behaved anomalously relative to its neighboring values and to values measured on other occasions. Time-of-flight and magnetic analysis of the extracted ion beam from CEBIS showed the presence of oxygen and nitrogen ions in the source. The presence of these ions was traced to a small leak in the CEBIS gas inlet system which was repaired. Subsequent charge state analysis of the incident ion beam showed only argon ions and protons in the beam.

Cross-section measurements require that the beam intensity of the various charge state fractions present be known accurately. The ions leaving the gas cell were detected either by a Faraday cup or by a channeltron electron multiplier operating in the current mode. In either case, the determination of the beam intensity was complicated by the pulsed nature of the ion output from the EBIS, and by the very high ion charge states present. The Faraday cup was a tube, 1 cm in diameter and 10 cm long, with the collector end cut at 45° and closed off by a 0.25-mm-thick gold sheet. The cup was inside a 2.5-cm-diam grounded tube which acted as an electrostatic shield. The Faraday cup signal was amplified by a Keithley Model 127 current-to-voltage amplifier. With the voltage-to-current amplifier time constant set at 10 μs and no signal present, the background noise produced a 1-V peak-to-peak signal on the 10^{11}-V/A scale. The Faraday cup was located 23 cm from the gas-cell exit, and beam profile scans obtained using the 1.0-mm-wide entrance slit of the moveable $\pi / \sqrt{2}$ cylindrical electrostatic analyzer as a scanner, showed that the entire 0.5-cm-diam beam was collected by the Faraday cup for each charge state. The Faraday cup intercepts ions scattered by $\pm 1.5°$, which, in light of the large projectile-to-target mass ratio in these experiments, and therefore small laboratory scattering angels, ensured that all projectiles scattered in capture were collected.

The channeltron output current was also amplified by a Keithley 127 current-to-voltage amplifier. The output pulses from both Keithly amplifiers were fed into a Tektronix 2430A digital oscilloscope. Figure 5 shows traces (averaged over 8 extracted EBIS pulses) of an Ar^{14+} direct beam pulse as detected by the Faraday cup, and by the channeltron electron multiplier, the latter after passing through the $\pi / \sqrt{2}$ cylindrical electrostatic analyzer. (Figure 5 is a composite of two oscilloscope traces taken at different times.)

It is known that highly charged ions striking surfaces produce copious amounts of secondary electrons due to the high potential energy of the ions (equal to the binding energy of the missing electrons) [11]. This potential energy ranges from 0.57 keV for Ar^{8+} to 5.84 keV for Ar^{16+} [23]. The design of the Faraday cup and its large length-to-diameter ratio ensure that the secondary electrons are collected if the ion beam is centered.
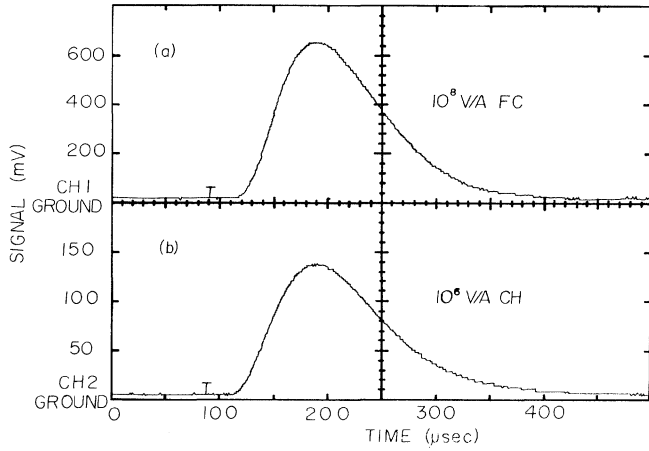
FIG. 5. Digital oscilloscope traces averaged over 8 extracted EBIS pulses of an Ar^{14+} direct beam pulse as detected (a) on a Faraday cup (FC), and (b) by a channeltron (CH) electron multiplier, the latter after passing through the $\pi/\sqrt{2}$ cylindrical electrostatic analyzer. The gain on the Faraday cup amplifier was 10^8 V/A, and that on the channeltron 10^6 V/A. The figure is a composite of two oscilloscope traces taken at different times.

The ion current recorded by the channeltron electron multiplier had to be corrected for the response of the multiplier to the different charge states which produce different amounts of secondary electrons. This correction is discussed below in more detail. To ensure that the channeltron, a high-current electron multiplier [24], could handle the ion currents and not saturate, the multiplier was operated between 1.2 and 1.8 kV, well below the manufacturer's recommended operating voltage of 3.0 kV. At these voltages, the channeltron peak output currents were kept below 1 μA. In addition, for each charge state, the recorded ion current pulse was compared with a time slice of this pulse, 100 times smaller, in order to verify the linear channeltron response. (The time slice was obtained by applying a 200-V dc potential to a pair of deflection plates inside CEBIS, and then dropping this potential to ground for 300 ns.)

III. RESULTS

A. Cross-section measurements and data analysis

As mentioned above, the cross sections in this work were determined using the growth-rate method. Two different measurements were taken to determine the charge state content in the beam after it passed through the gas cell. In the first measurement, the ion beam was charge state analyzed by the energy-retardation method [10,25]. Figure 2 shows the experimental arrangement used, and Fig. 6 shows a typical energy-retardation scan for Ar^{13+} on H_2. The Faraday cup ion pulses (Fig. 5) were averaged over 16 extracted CEBIS pulses and integrated over time by the digital oscilloscope. For a charge state q, the Faraday cup signal $Q_q = q A_q \int \overline{N_q(t)} dt \equiv q A_q N_q$, where A_q is the amplifier gain for charge state q, and $\overline{N_q(t)}$ is the average over 16 CEBIS pulses $N_q(t)$.
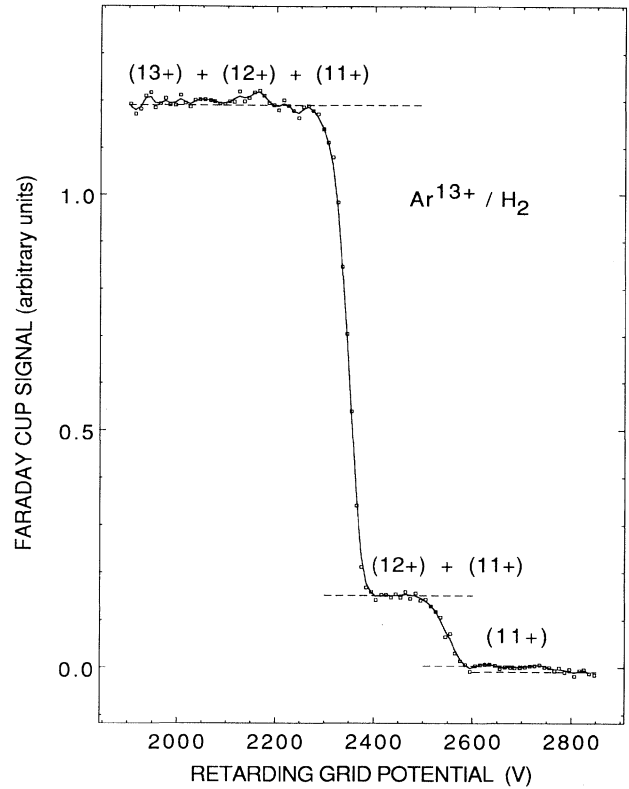

FIG. 6. A typical energy-retardation scan for Ar^{13+} on H_2.

For retarding grid potentials $V_{ret} \leq 2.3$ kV (the ion extraction potential), the recorded ion signal at a given target thickness ρ, is

$$Q_1(\rho) = q A_q N_q(\rho) + (q-1) A_{q-1} N_{q-1}(\rho)$$
$$+ (q-2) A_{q-2} N_{q-2}(\rho) \ .$$

Around 2.3 kV applied to the retarding grids, ions of charge q are blocked, but ions whose charge has decreased by one or more units in a charge changing collision have a higher kinetic energy per charge and pass through. [The exact potential at which ions of charge q are blocked depends on the depth of the potential depression between the drift tubes and the center of the electron beam in the EBIS. This depression in turn depends on the electron-beam current and the electron-beam radius, which is not known. For a 17-mA, 3.8-keV electron beam, assuming an electron-beam current density of 500 A/cm^2 together with 15% neutralization of the electron-beam space charge by ions trapped in the beam, the electron-beam radius is 3.3×10^{-2} mm, and for 8-mm-diam drift tubes, the potential drop from the drift tube to the center of the electron beam is 40 V. The potential drop therefore determines the uncertainty in the incident ion energy, which we believe to be $(2.30^{+0}_{-0.05})q$ keV.]

For $V_{ret} \leq V \leq (V_{ret})(q/q-1)$, the detected ion signal is

$$Q_2(\rho) = (q-1) A_{q-1} N_{q-1}(\rho) + (q-2) A_{q-2} N_{q-2}(\rho) \ ,$$

and   for $V_{ret}(q/q-1) \leq V \leq (V_{ret})(q/q-2)$, $Q_3(\rho)$

$=(q-2)A_{q-2}N_{q-2}(\rho)$. The measured signals $Q_1(\rho)$, $Q_2(\rho)$, and $Q_3(\rho)$, recorded at the same amplifier gain A, then determine $N_q(\rho)=[Q_1(\rho)-Q_2(\rho)]/q$, $N_{q-1}(\rho)=[Q_2(\rho)-Q_3(\rho)]/(q-1)$, and $N_{q-2}(\rho)=[Q_3(\rho)-Q_n(\rho)]/(q-2)$, where Q_n is the amplifier input noise. The total number of particles in the incident ion beam is given by $N_0=N_q(\rho)+N_{q-1}(\rho)+N_{q-2}(\rho)$ and is independent of pressure. In the linear approximation,

$$\sigma_{q,q-1}=\frac{N_{q-1}}{N_0}\frac{1}{\rho}$$

$$=\frac{q(q-2)[Q_2(\rho)-Q_3(\rho)]}{(q-1)(q-2)Q_1+(q-2)Q_2+qQ_3}\frac{1}{\rho}, \quad \text{etc.}$$

$$(9)$$

In the second type of measurement, the ion beam leaving the gas cell was charge state analyzed by a $\pi/\sqrt{2}$ cylindrical electrostatic analyzer. For each projectile charge state incident on the gas cell, the moveable analyzer platform was positioned to place the analyzer entrance slit on the axis of the gas cell. With no gas in the cell, the beam position was then adjusted to give the maximum transmitted ion current through the analyzer which was set to analyze ions at the extracted beam voltage. With gas in the cell, the channeltron output pulses were recorded as a function of the $\pi/\sqrt{2}$ analyzer voltage V_a for different target thickness ρ. As in the above-mentioned energy-retardation method, the channeltron output pulses [Fig. 5(a)] were averaged over 16 extracted CEBIS ion pulses and integrated over time by the digital oscilloscope. In this case, however, $Q_q=qA_qN_q\delta_qG$, where δ_q is the number of secondary electrons released by an ion of charge q incident on the channeltron, G is the gain of the channeltron, and the rest of the symbols are the same as above. Plots of the collected channeltron output charge versus the analyzer voltage at a given target pressure shows three peaks which corresponds to the direct, and one- and two-electron transfer components of
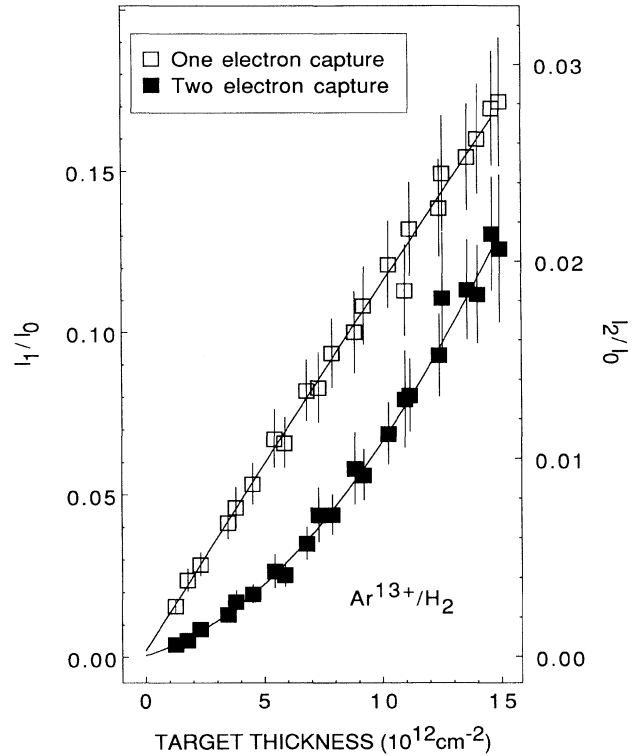

FIG. 7. One- and two-electron transfer charge fraction growth with pressure for Ar^{13+} on H_2 as measured with the $\pi/\sqrt{2}$ cylindrical electrostatic analyzer. The data are corrected for the channeltron response to different charge states.

the beam. Figure 7 shows the growth of the one- and two-electron transfer components of the beam for Ar^{13+} on H_2 after correction for channeltron response to different charge states, see below.

The cross sections were extracted from the data as follows. Let

$$f_{q-1}(\rho)\equiv\frac{N_{q-1}(\rho)}{N_q(\rho)+N_{q-1}(\rho)+N_{q-2}(\rho)}=\frac{Q^{ch}_{q-1}(\rho)R_{q/q-1}}{\frac{A_{q-1}}{A_q}Q^{ch}_q(\rho)+Q^{ch}_{q-1}(\rho)R_{q/q-1}+\frac{A_{q-1}}{A_{q-2}}Q^{ch}_{q-2}(\rho)R_{q/q-2}},$$

$$f_{q-2}(\rho)\equiv\frac{N_{q-2}(\rho)}{N_q(\rho)+N_{q-1}(\rho)+N_{q-2}(\rho)}=\frac{Q^{ch}_{q-2}(\rho)R_{q/q-2}}{\frac{A_{q-1}}{A_q}Q^{ch}_q(\rho)+Q^{ch}_{q-1}(\rho)R_{q/q-1}+\frac{A_{q-1}}{A_{q-2}}Q^{ch}_{q-2}(\rho)R_{q/q-2}},$$

$$(10)$$

where $R_{q/q-r}$ is the channeltron response of charge state $q-r$ relative to q, etc., and is equal to $R_{q/q-1}=q\delta q/[(q-1)\delta_{q-1}]$.

The different ion charge state signals were of different amplitude, and to record signals that were more or less of the same magnitude, either the voltage applied to the channeltron or the amplifier gain A has to be adjusted. Since the amplifier gain is known, the gain was varied and appears in expressions (10).

Unfortunately, the channeltron responses $R_{q/q-r}$ of charge state $q-r$ relative to q are not known, and no direct, unambiguous, and reproducible determination of these quantities could be made. Accordingly, in these measurements, the following analysis was done. In the first pass through the data for a given projectile charge state q, all the $R_{q/q-1}$'s in (10) were set equal to 1, and the resulting $f_q(\rho)$'s were plotted versus ρ. (The plots obtained are similar to those shown in Fig. 7.) From the

TABLE I. Ar^{q+} on He cross sections at $2.3q$ keV (10^{-16} cm^2).

| q | $\sigma_{q,q-1}$ | | | | This work | |
	This work	Ref. [35][a]	Ref. [3][b]	Ref. [7][c]	$\sigma_{q,q-2}$	$\sigma_{q,tot}$
8	22.1±3.2	30.0	17.0±3.3	14.4±2.9	8.0±1.2	30.1±4.3
9	30.4±4.2		21.8±5.5	34.6±6.9	<0.3	30.7±4.2
10	33.1±4.5			32.0±6.4	0.7±0.2	33.8±4.6
11	37.2±4.8			27.0±5.4	<0.3	37.5±5.0
12	45.1±6.1			40.5±8.1	<0.2	45.3±6.3
13	46.2±6.1			32.8±6.5	0.9±0.7	47.1±6.3
14	46.7±6.2			34.0±6.8	2.6±1.9	49.3±6.6
15	48.6±6.6			27.3±5.5	1.8±1.0	50.4±6.9
16	50.4±7.3				1.5±0.8	51.9±7.5

[a]Reference [35] measured at $3.75q$ keV.
[b]Reference [3] measured at $0.5q$ keV.
[c]Reference [7] measured at $0.198q$ keV. For the data of Ref. [7] we show the total uncertainty of the measurement instead of the statistical reproducibility.

plots, uncorrected cross sections were extracted by least squares fitting a second-order polynomial $f_q(\rho)=a_1\rho+a_2\rho^2$ to the data. The linear term a_1 is directly related to the cross section of interest, and the quadratic term a_2 is related to various cross sections as can be seen by inspecting the coefficients of the quadratic terms in Eq. (3). The single charge changing cross sections so obtained always followed the trend of those obtained by the energy-retarding method but were lower in value. Taking the latter as more representative of the true values, the relative responses $R_{q/q-1}$ of charge state $q-1$ relative to q, etc., were obtained. (The response of the channeltron to charge state q is always greater than to $q-1$, and hence the $R_{q/q-1}$'s are greater than 1, typically 1.2–1.3.) Then, taking $R_{q/q-2}=R_{q/q-1}R_{q-1/q-2}\cong R^2_{q/q-1}$ the $R_{q/q-r}$ values were put into Eq. (10), other values of $f_q(\rho)$'s were obtained and the process repeated until the cross section obtained at a comparison pressure $P_c=4.3\times10^{-5}$ mbar agreed with the retarding grid value. At this point, the coefficients of $f_p(\rho)$ determined the cross sections. The cross sections so extracted are listed in Tables I and II and shown plotted against the charge on the projectile in Figs. 8 and 9. In addition to our values, we list some of the experimentally measured total cross sections, together with their errors, that have appeared in the literature. (If the values and error bars were not stated explicitly, we extracted them from graphs in the mentioned articles.) We have included only those measurements that gave some indication of the experimental errors involved.

B. Discussion of results and comparison with theory and other experiments

Generally, atomic cross sections are measured under experimental conditions for which only a single collision takes place in the target. Such conditions are assured if linear attenuation and/or linear growth of a charge state fraction occurs as a function of target thickness (pressure). As Fig. 7 shows, at a pressure of 4.3×10^{-5} mbar, or at a target thickness of 9.7×10^{12} cm^{-2}, the one-

electron transfer cross section is linear, while the two-electron transfer cross section is not.

The reason for this is due to the large disparity in magnitudes of the one- and two-electron transfer cross sections. That the observed behavior is indeed what one would expect was tested as follows. Equations (2) were used to generate mock data, i.e., $N_q(\rho)/N_0$ vs ρ curves using the experimentally measured cross sections and the actual pressure values used in the experiment. Figure 10 shows such mock data for Ar^{13+} on H_2. The agreement with the actual data, Fig. 7, corrected for the channeltron response is quite good. These curves were then analyzed by least squares fitting a second-order polynomial to the mock data. The extracted cross sections agreed with the original values fed in, as well as with the expressions given in Eq. (3) for the coefficient of the second-order term in ρ.

In the past decade, a number of semiclassical close-coupling calculations of total and partial cross sections have been performed [26–33]. However, these have been

TABLE II. Ar^{q+} on H_2 cross sections at $2.3q$ keV (10^{-16} cm^2).

| q | $\sigma_{q,q-1}$ | | | This work | |
	This work	Ref. [7][a]	Ref. [6][b]	$\sigma_{q,q-2}$	$\sigma_{q,tot}$
8	69.8±5.6	65.0±13.0	48.1±2.8	3.1±1.0	72.9±5.9
9	77.0±6.1	97.3±19.5	56.3±4.6	1.4±0.6	78.4±6.4
10	76.9±6.4	73.3±14.7	59.7±7.3	1.4±1.3	78.3±6.6
11	88.9±7.2	105.0±21.0		4.6±1.6	93.5±7.5
12	92.1±7.4	102.0±20.4		2.1±1.0	94.2±7.6
13	104.1±8.7	96.3±19.3		5.7±3.1	109.8±9.7
14	98.9±8.6	105.5±21.1		5.0±1.9	103.9±9.4
15	113.5±10.2	97.0±19.4		3.1±2.3	116.6±10.4
16	118.0±10.5			3.3±2.2	121.3±10.6

[a]Reference [7] measured at $0.198q$ keV. For the data of Ref. [7] we show the total uncertainty of the measurement instead of the statistical reproducibility.
[b]Reference [6] measured at $2.0q$ keV.

limited to C^{q+} and O^{q+} on H and He. The only calcula-
tions of Ar^{8+} on He that we are aware of were done by
Kimura and Olson [34] who carried out a molecular-
structure calculation of the $(ArHe)^{8+}$ system using the

pseudopotential method. The total and partial one-
electron capture cross sections for capture into the Ar^{7+}
$4d$ and $4f$ states were calculated by the perturbed-
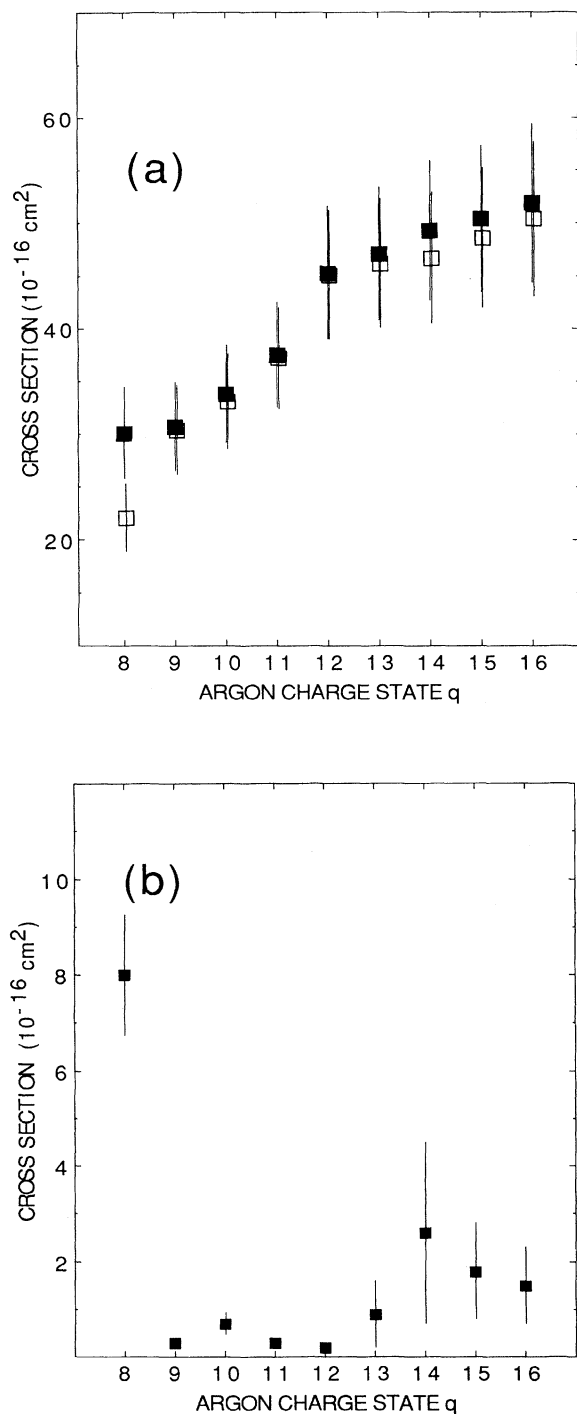stationary-state method along straight line trajectories.

FIG. 8. (a) Total (solid squares) and one-electron (open
squares) transfer cross sections for Ar^{q+} on He at $2.3q$ keV as a
function of argon-ion charge, and (b) two-electron transfer cross
sections.
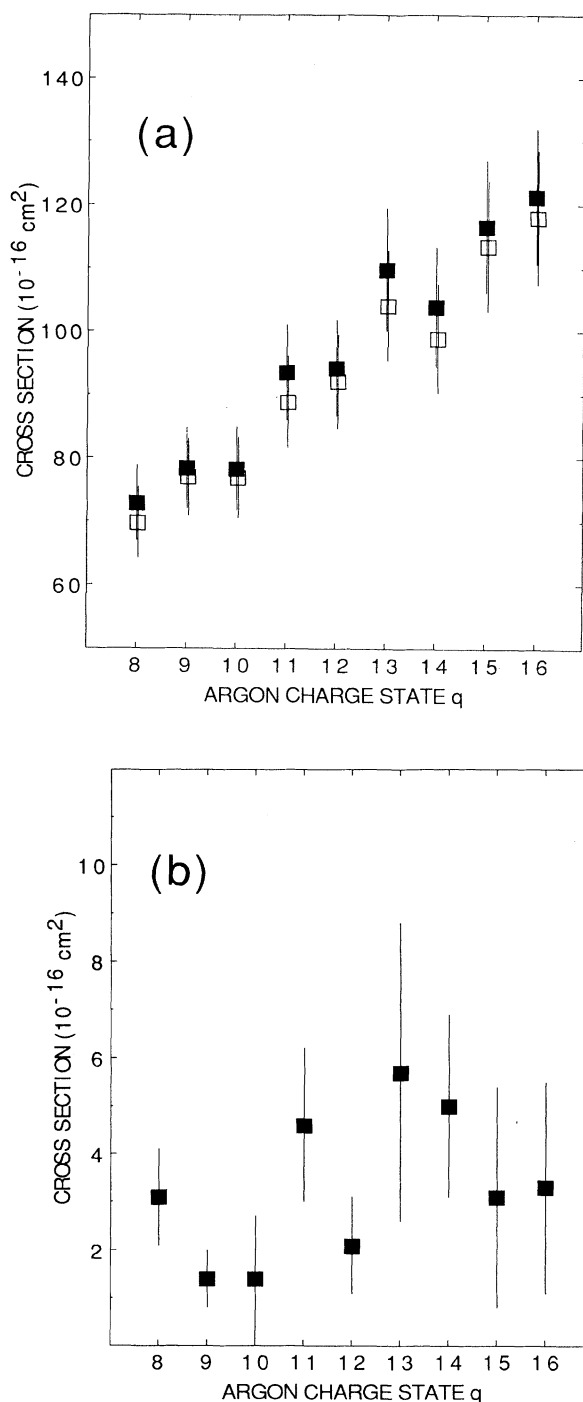
FIG. 9. (a) Total (solid squares) and one-electron (open
squares) transfer cross sections for Ar^{q+} on H_2 at $2.3q$ keV as a
function of argon-ion charge, and (b) two-electron transfer cross
sections.

In the calculation, only single-electron excitations in the possible configurations of the pseudo-two-electron system were used. Their calculated cross sections are redrawn in Fig. 11 together with our single data point, the solid circle. The open circles are data from Justiniano et al. [3], the solid square is from Mann [7], and the open square is from Salzborn and Muller [35]. In all cases the data points are for single-electron capture without regard as to the final charge state of the helium atom.

It is interesting to compare the cross sections calculated according to the absorbing sphere model [36] with our data. For a system in which the initial channel crosses a large number of possible final channels, one can assume a unit probability for the reaction occurring inside some critical distance R_c. Then, the total cross section is given by $\sigma = \pi R_c^2$ [36,37]. The critical distance R_c can be determined from the relation [36]

$$R_c^2 \exp(-2.648\alpha R_c / z^{1/2}) = (2.864 \times 10^4) z(z-1) v_0 , \tag{11}$$

where $\alpha = [I_t(\text{eV})/13.6]^{1/2}$, I_t is the ionization potential of the target atom, z the charge on the projectile, and v_0 the relative velocity. Both R_c and v_0 are in atomic units, and for H_2, the Franck-Condon factor is taken as 1. The absorbing sphere cross sections calculated for $2.3q$-keV argon ions incident on He and H_2 were multiplied by 0.565 and 0.747, respectively, to normalize them to our
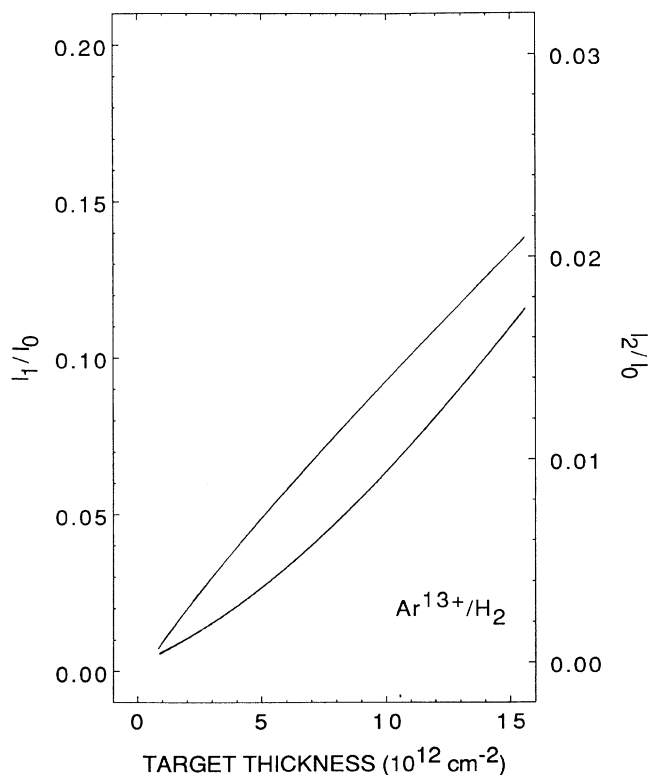

FIG. 11. Kimura and Olson's calculated total and partial cross sections for single-electron capture in Ar^{8+} + He collisions, adapted from Ref. [34]. The solid point is our measurement at 0.46 keV/amu, the open circles are data from Ref. [3], the solid square is from Ref. [7], and the open square is from Ref. [35]. All measurements are for single-electron capture without regard for the charge state of the He ion.

experimental cross sections for Ar^{8+}. They are shown in Fig. 12, together with the experimental data. The general shape of the calculated cross section agrees quite well with the data, although the magnitude does not. The only adjustable quantity in the absorbing sphere cross-

FIG. 10. Mock single and double charge transfer growths with pressure for Ar^{13+} on H_2 generated from Eq. (2), for a 12.2-cm target and experimentally measured total cross sections and pressures used. Compare with Fig. 7.
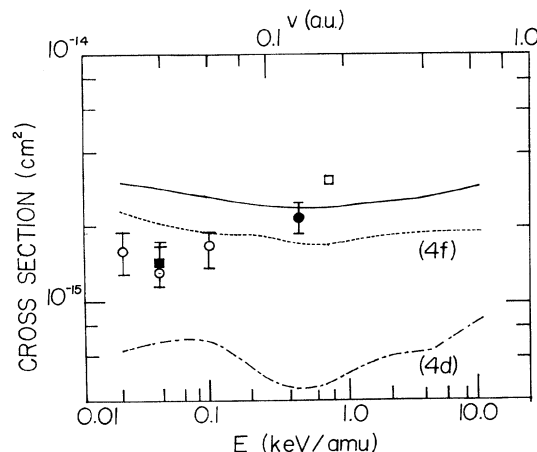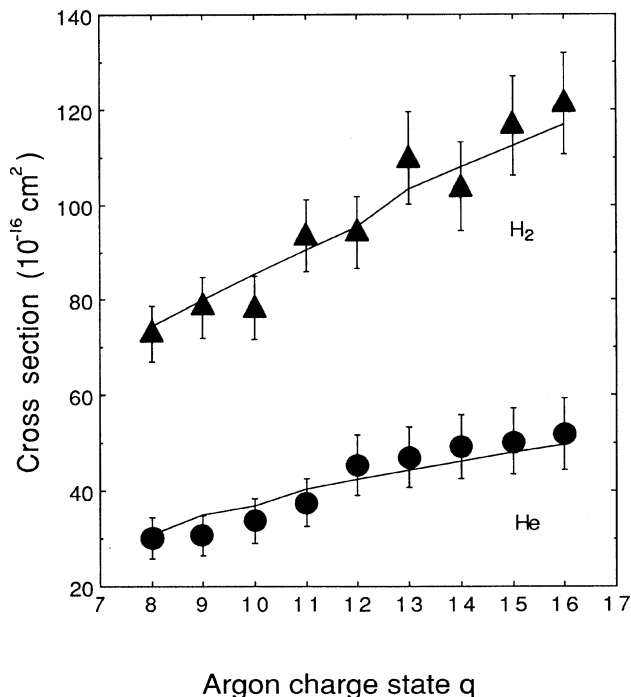

FIG. 12. Comparison of our total cross-section data for Ar^{q+} on He and H_2 at $2.3q$ keV with the cross sections calculated according to the absorbing sphere model of Olson and Salop [36]. The absorbing sphere cross sections were multiplied by 0.565 and 0.747 in order to normalize them to the experimental values of Ar^{8+} on He and H_2, respectively.

section calculation is the matrix element $H_{12} = 9.13 \exp(-1.324\alpha R_c / z^{1/2})$ which was obtained from a fit to a large number of calculated stripped-ion–atomic-hydrogen system $H_{12}s$ [36]. If the values of 9.13 and 1.324 are both increased by 18%, the magnitudes of the calculated cross sections approach the experimental values, but the overall agreement with the data is not as good as with the original values.

When comparing our data in Tables I and II with those of others, it should be borne in mind that all sets were measured at different collision energies. According to the absorbing sphere model, the cross section should rise with decreasing collision velocity [38]. However, the cross sections measured by Justiniano et al. [3] and Mann [7] at lower collision energies are clearly smaller than ours. If we look at the energy dependence of the measured Ar^{8+}-He data, shown in Fig. 11, which was measured by four different groups, there is a clear pattern emerging and all the data appear consistent with one another. It is quite possible that the difference between our data and Mann's is due to energy variation of the cross section. At least, the Ar^{8+} on He values would indicate as such. However, the Ar^{q+} on H_2 $(8 \leq q \leq 10)$ data obtained by Can et al. [6], at $2.0q$ keV is much closer in energy to our data, and their measured cross sections appear to be too low.

In previous work [3,35] the reported Ar^{q+} cross sections for double capture from He are about a factor of 10 lower than single capture cross sections. Our measured double capture cross sections are significantly lower. Since the single capture values are in general agreement with those reported by others, and the behavior of the double capture cross sections with pressure is in agreement with that calculated on the basis of Eqs. (2) for given values of all pertinent cross sections, we are at a loss to explain this discrepancy.

[1] Y. Jongen and C. M. Lyneis, in The Physics and Technology of Ion Sources, edited by I. G. Brown (Wiley, New York, 1989), p. 207.

[2] E. D. Donets, in The Physics and Technology of Ion Sources, edited by I. G. Brown (Wiley, New York, 1989), p. 245.

[3] E. Justiniano, C. L. Cocke, T. J. Grey, R. Dubois, W. Waggoner, R. Schuch, H. Schmidt-Bocking, and H. Ingmersen, Phys. Rev. A 29, 1088 (1984).

[4] T. Iwai, Y. Kaneko, M. Kimura, N. Kobayashi, A. Matsumoto, S. Ohtani, K. Okuno, S. Takagi, H. Tawara, and S. Tsurubuchi, J. Phys. B 17, L95 (1984).

[5] H. Tawara, T. Iwai, Y. Kaneko, M. Kimura, N. Kobayashi, A. Matsumoto, S. Ohtani, K. Okuno, S. Takagi, and S. Tsurubuchi, J. Phys. B 18, 337 (1985).

[6] C. Can, T. J. Gray, S. L. Varghese, J. M. Hall, and L. N. Tunnell, Phys. Rev. A 31, 72 (1985).

[7] R. Mann, Z. Phys. D 3, 85 (1986).

[8] H. Andersson, G. Astner, and H. Cederquist, J. Phys. B 21, L187 (1988).

[9] H. Cederquist et al., Phys. Rev. Lett. 62, 1465 (1989).

[10] H. Tawara and A. Russek, Rev. Mod. Phys. 45, 178 (1973).

[11] H. J. Andra, in Physics of Highly-Ionized Atoms, Vol. 201 of NATO Advanced Study Institute, Series B: Physics, edited by R. Marrus (Plenum, New York 1989), p. 377.

[12] C. L. Cocke, R. DuBois, T. J. Gray, E. Justiniano, and C. Can, Phys. Rev. Lett. 46, 1671 (1981).

[13] V. O. Kostroun, in Proceedings of the International Symposium on Electron Beam Ion Sources and their Applications, edited by A. Hershcovitch, AIP Conf. Proc. No. 188 (AIP, New York, 1989), p. 65.

[14] K. E. Poulter, J. Phys. E 10, 112 (1977).

[15] MKS Instruments Bulletin H/A-12/89, MKS Instruments, Inc., Andover, MA 01810.

[16] N. A. Florescu, in Transactions of the Eighth National Vacuum Symposium, edited by L. E. Preuss (Pergamon, Oxford, 1962), Vol. 1, p. 504.

[17] A. Berman, J. Appl. Phys. 36, 3356 (1965).

[18] MKS Instruments, Inc., Andover, MA 01810.

[19] Granville Phillips Co., Boulder, CO 80303.

[20] L. H. Toburen, Ph.D. thesis, Vanderbilt University, 1967, Appendix II (unpublished).

[21] A. Muller, H. Klinger, and E. Salzborn, J. Phys. B 9, 291 (1976).

[22] A. Muller, H. Klinger and E. Salzborn, Nucl. Instrum. Methods 140, 181 (1977).

[23] Calculated using the MCHF program of C. Froese-Fischer, Comput. Phys. Commun. 43, 355 (1987).

[24] Galileo Model 4730, Galileo Electro-Optics Corp., Sturbridge, MA 01518.

[25] V. F. Kozlov and A. M. Rozhkov, Zh. Tekh. Fiz. 32, 719 (1962) [Tech. Phys. 7, 524 (1962)].

[26] M. Kimura, H. Sato, and R. E. Olson, Phys. Rev. A 28, 2085 (1983).

[27] M. Kimura and R. E. Olson, J. Phys. B 17, L713 (1984).

[28] F. Fritsch and C. D. Lin, Phys. Rev. A 29, 3039 (1984).

[29] M. Kimura and C. D. Lin, Phys. Rev. A 31, 590 (1985).

[30] M. Kimura and C. D. Lin, Phys. Rev. A 32, 1357 (1985).

[31] F. Fritsch and C. D. Lin, J. Phys. B 19, 2683, (1986).

[32] M. Kimura and N. F. Lane, Adv. At. Mol. Opt. Phys. 26, 79 (1990).

[33] F. Fritsch and C. D. Lin, Phys. Rep. 202, 1 (1991).

[34] M. Kimura and R. E. Olson, Phys. Rev. A 31, 489 (1985).

[35] E. Salzborn and A. Muller, in Electronic and Atomic Collisions, edited by N. Oda and K. Takayanagi (North-Holland, Amsterdam, 1980), p. 407.

[36] R. E. Olson and A. Salop, Phys. Rev. A 13, 579 (1976).

[37] N. F. Mott and H. S. W. Massey, The Theory of Atomic Collisions, 3rd ed. (Clarendon, Oxford, 1965), p. 188.

[38] R. E. Olson, J. Chem. Phys. 56, 2979 (1972).